Figure S1

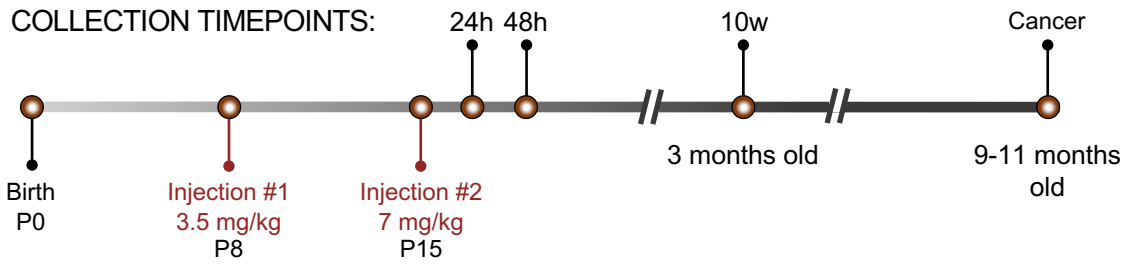

Figure S1. NDMA treatment regimen and collection timepoints, related to STAR Methods. A total of 10.5 mg/kg NDMA was injected in a split dose in neonatal mice, with 3.5 mg/kg injected at 8 days of age and 10 mg/kg injected at 15 days of age. Control mice were injected with equivalent volumes of saline at the same timepoints. Analyses were performed 24h, 48h, 10 weeks, and 9-11 months after the second injection.

Figure S2

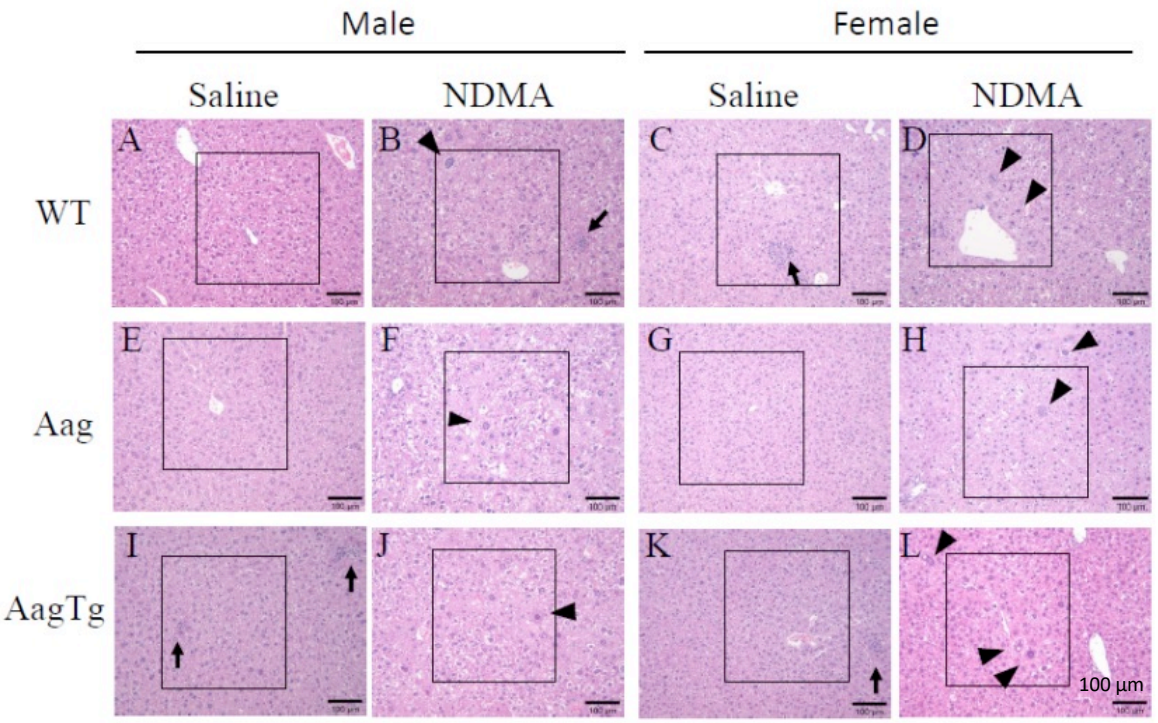

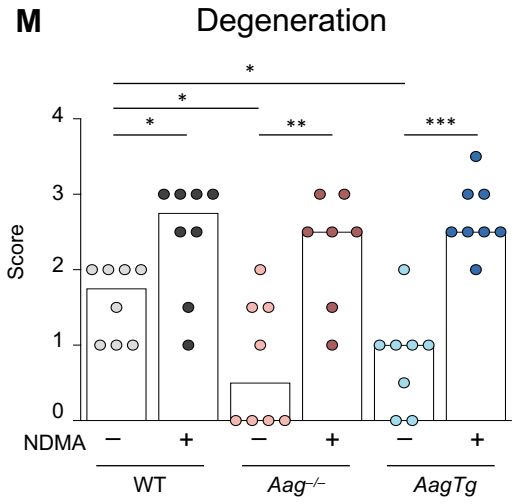

Figure S2. Livers of NDMA-treated mice show evidence of hepatocellular degeneration and hypertrophy 10 weeks after exposure, but not neoplasia, related to Figure 1. A &D) Representative hematoxylin and eosin (H&E) sections of liver from WT mice showed centrilobular (squares) to midzonal areas of hepatocellular degeneration and hypertrophy with and without karyomegaly (arrowheads) and intranuclear invaginations. Similar hepatocellular changes were noted in sections of livers from NDMA-treated *Aag*$^{-/-}$ (F & H) and *AagTg* mice (J & L). Sections of livers from control WT mice (A & C), *Aag*$^{-/-}$ (F & H), and *AagTg* (I & K) were within normal limits. Kupffer cell aggregates were present in control and treated groups (arrows). No significant foci of hepatocellular alteration were observed in any tissue. Original magnification x400, scale bars = 50 µm. M) NDMA significantly induced hepatocellular degeneration in all genotypes. Bar graphs show the median with data points representing individual animals, n = 8. Mann-Whitney *U*-test, $^{**}p < 0.01$, $^{***}p < 0.001$, $^{\#}p < 0.0001$.

Figure S3

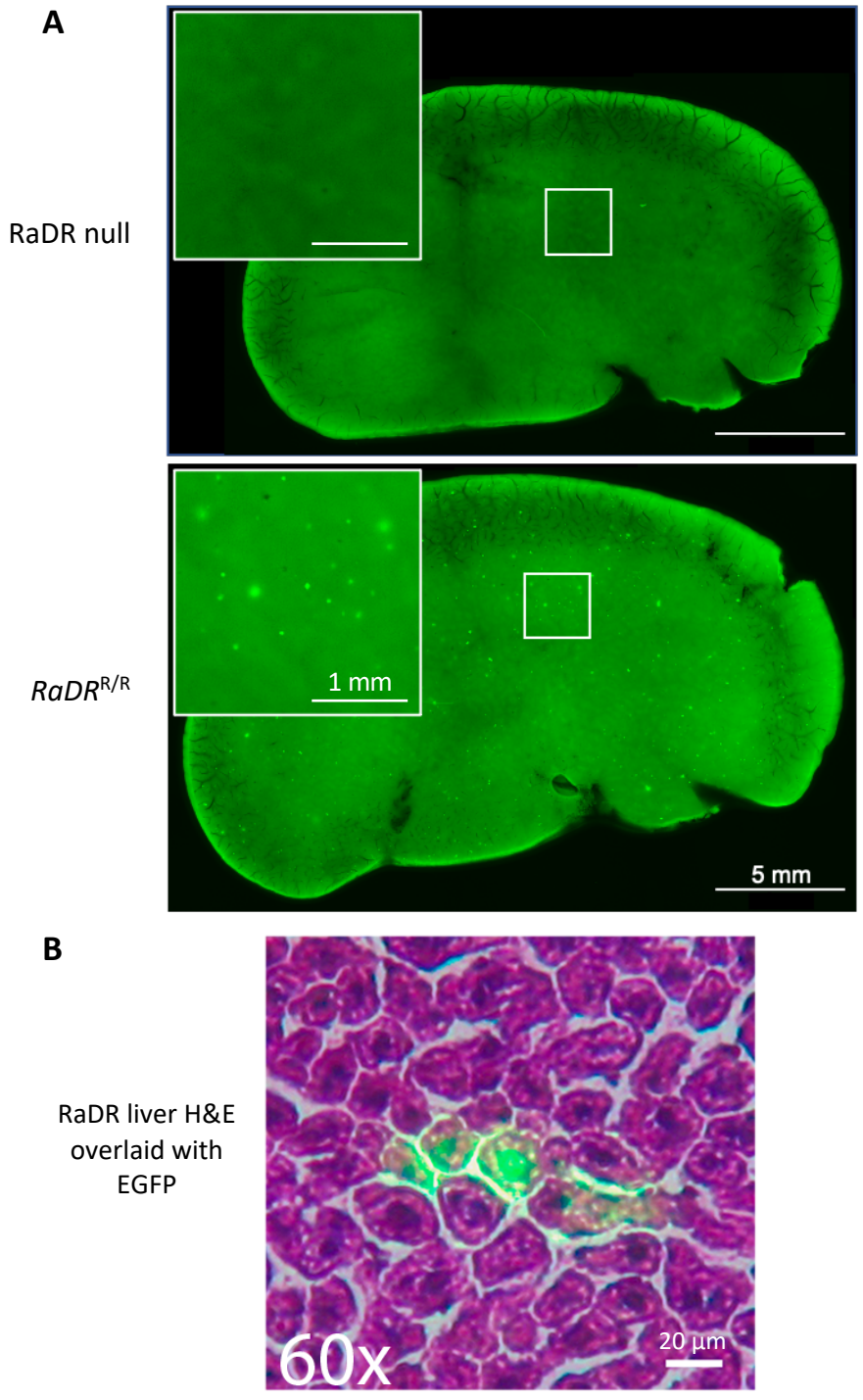

Figure S3. RaDR mice enable visualization of mutant cells in the liver by fluorescence microscopy, related to Figure 1 and STAR Methods. A) Whole-mount microscopy of EGFP in untreated RaDR null and *RaDR*$^{R/R}$ livers. Spontaneous recombinogenic mutations are visible as fluorescent foci in RaDR tissues, but not in mice without the RaDR transgene. Large image scale bar = 5 mm, inset scale bar = 1 mm. B) Mutant hepatocyes are visible in an overlay of EGFP and H&E. Scale bar = 20 µm. Hepatocyte H&E overlay reused from Sukup-Jackson et al., PLOS Genetics, 2014, https://doi.org/10.1371/journal.pgen.1004299 under Creative Commons license CC BY 4.0. This image was cropped from a larger figure.

Figure S4

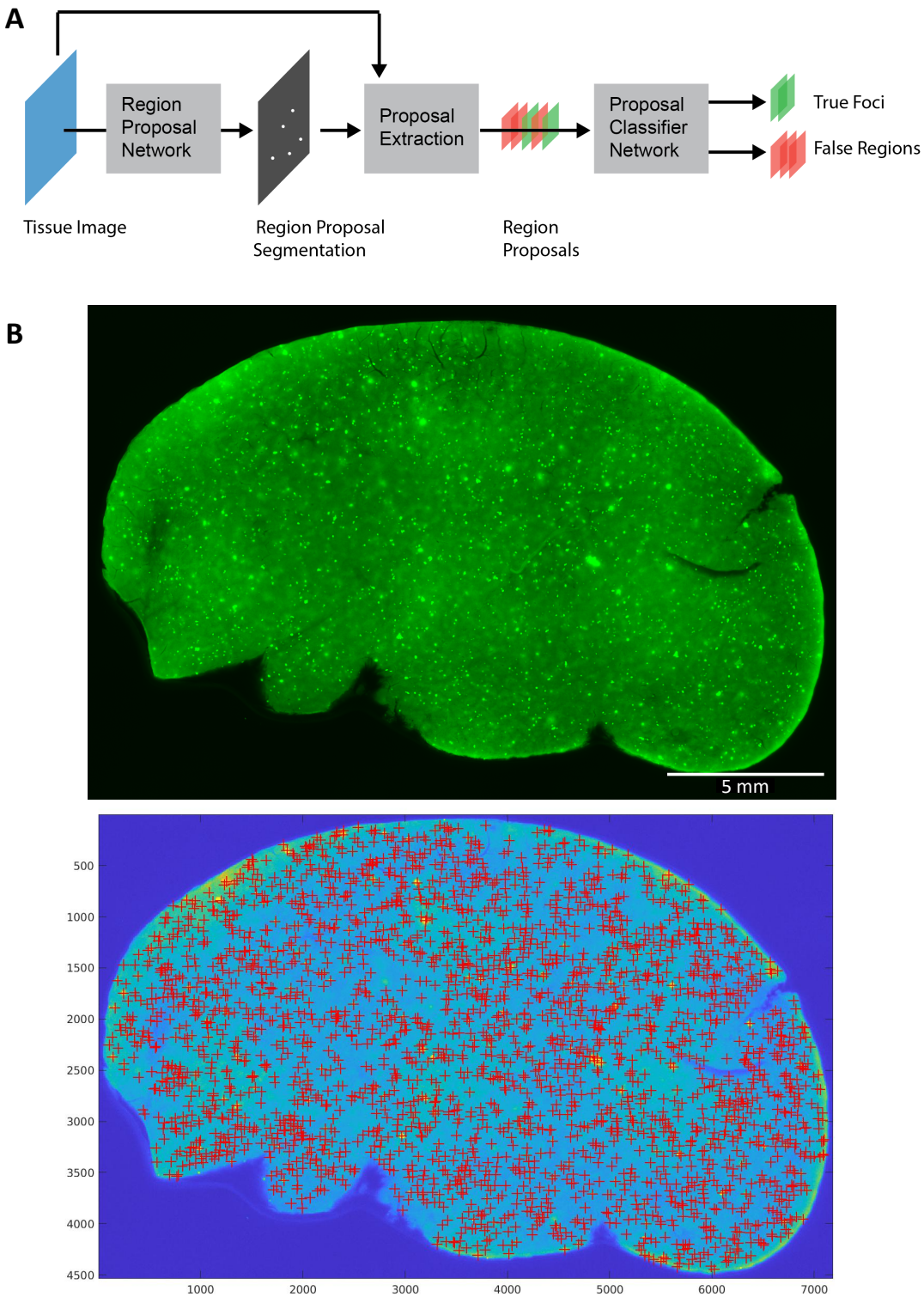

Figure S4. Machine learning network for automated enumeration of fluorescent foci in RaDR tissues, related to STAR Methods. A) Schematic of foci counting algorithm. See STAR methods for details. B) Sample RaDR liver image (top) and foci counting algorithm output (bottom).

Figure S5

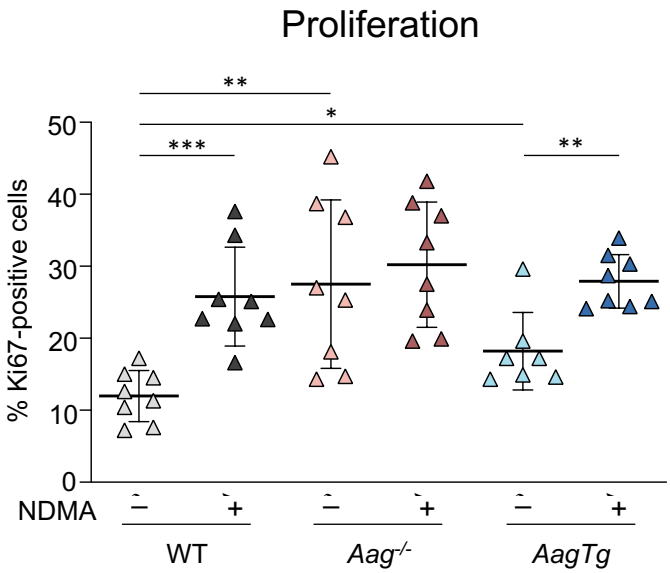

Figure S5. Proliferation is not significantly different among NDMA-treated mice 48h post-exposure, related to Figure 2. The proportion of proliferating cells was determined by flow cytometry of Ki67-positive cells. Data represented as mean ± SD. Each data point represents one mouse, n = 8 except *AagTg* saline where n = 7. Statistical comparisons calculated by unpaired Student's *t*-test, *$p < 0.05$, **$p < 0.01$, ***$p < 0.001$.

Figure S6

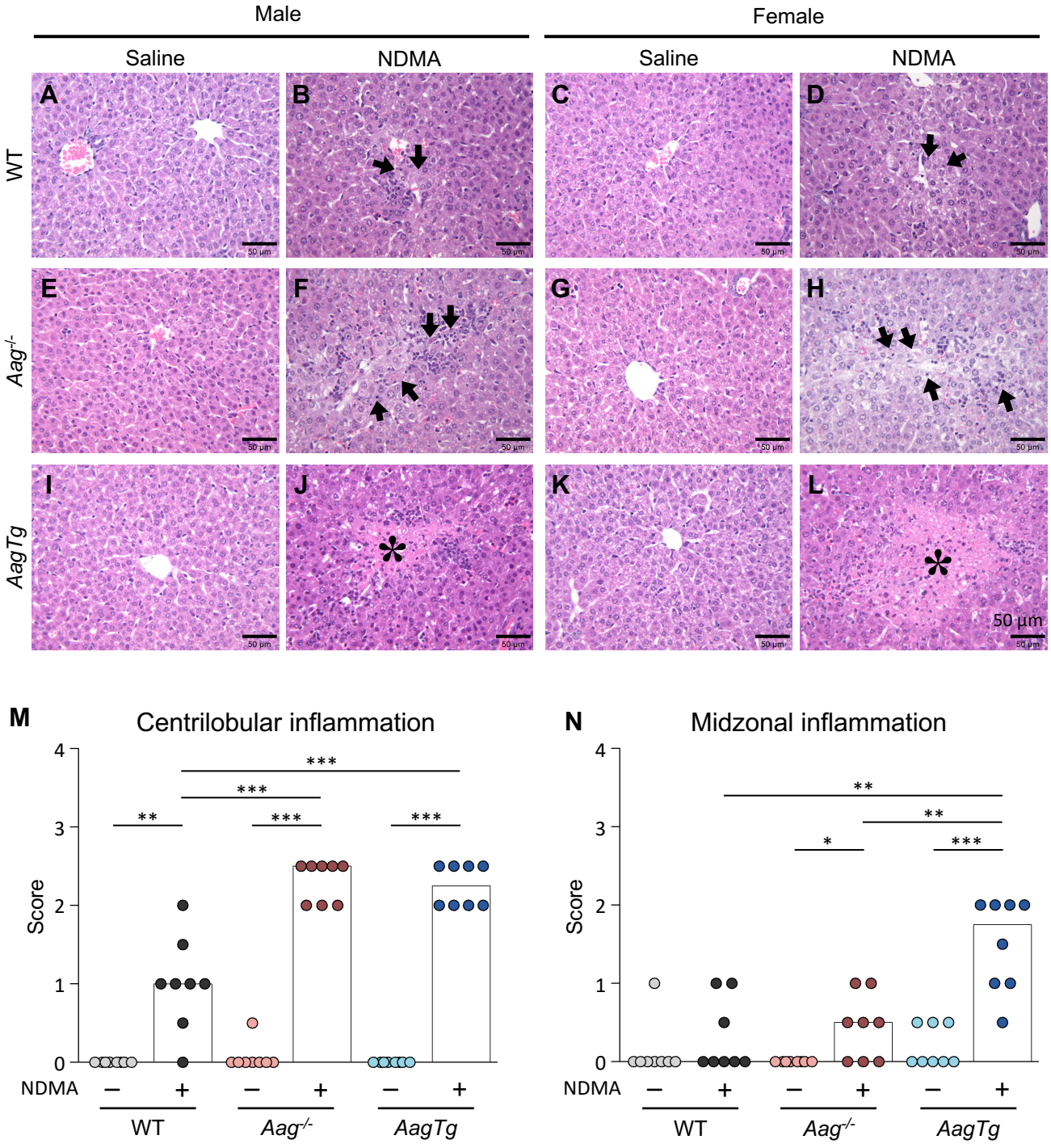

Figure S6. Acute periacinar hepatocellular damage is more pronounced in *AagTg* mice at 24h post-NDMA treatment, related to Figure 3. A–D) Representative H&E staining of liver sections from WT mice show individual necrotic hepatocytes (arrowheads) and numerous degenerate hepatocytes surrounding a central vein in NDMA treated mice (B&D). E–H) Sections of liver from *Aag*$^{-/-}$ mice exhibited multifocal areas of mild centrilobular necrosis and degeneration (arrows) with low numbers of macrophages and fewer neutrophils at the periphery. I–L) Sections of liver from *AagTg* mice show larger areas of centrilobular (periacinar) hepatocellular necrosis (asterisk) and degeneration surrounded by low numbers of macrophages. No histopathologic changes were noted in sections of liver from control WT (A & C), *Aag*$^{-/-}$ (F & H), and *AagTg* mice (I & K). Original magnification x400, scale bars = 50 µm. M & N) Leukocytic infiltration scores in centrilobular (M) and midzonal (N) regions in the liver. Bars indicate the median of scores from individual mice, n = 8. Mann-Whitney *U*-test, **p* < 0.05, ***p* < 0.01, ****p* < 0.001, $^{\#}$*p* < 0.0001.

Figure S7

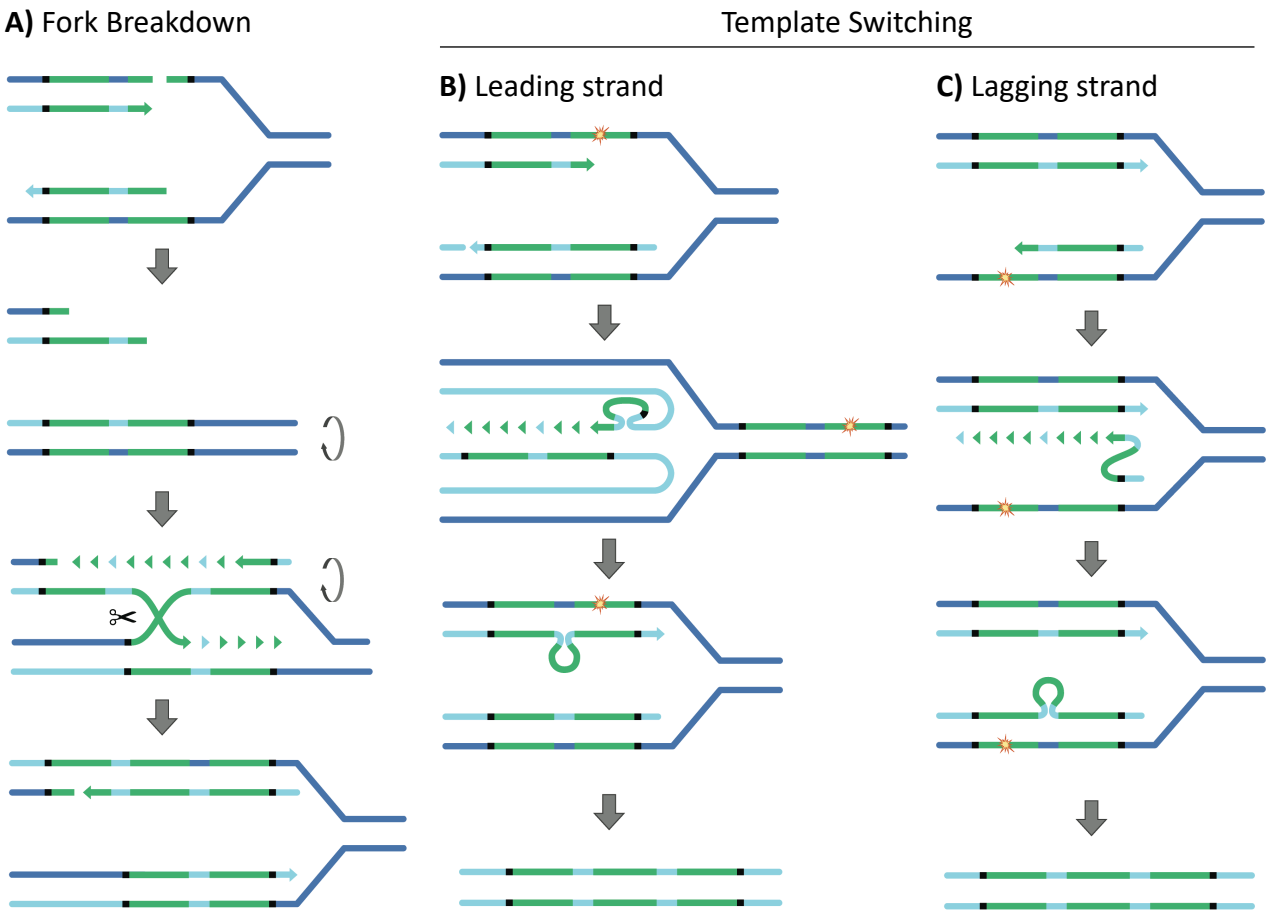

Figure S7. Mechanisms to produce EGFP within the RaDR transgene at replication forks, related to Figure 1. A) Fork breakdown at an SSB can be restored by HR to reconstitute full-length EGFP cDNA (green segments) within the RaDR transgene (black boxes indicate deleted sequences). B) Replication blocks in the leading strand can lead to template switching by fork reversal, potentially leading to production of full-length EGFP in the RaDR transgene. C) Replication blocks in the lagging strand can be bypassed by utilizing the nascent strand on the sister chromatid as a template for synthesis. Template switching potentially leading to production of full-length EGFP in the RaDR transgene (D-loop in step 2 not shown).